Combined Hyperpolarized 13C-pyruvate MRS and 18F-FDG PET (HyperPET) Estimates of Glycolysis in Canine Cancer Patients

Hansen, Adam E.; Gutte, Henrik; Holst, Pernille; Johannesen, Helle H.; Rahbek, Sofie; Clemmensen, Andreas E.; Larsen, Majbritt M.E.; Schøier, Christina; Ardenkjær-Larsen, Jan Henrik; Klausen, Thomas L.; Kristensen, Annemarie T.; Kjær, Andreas

Published in:
European Journal of Radiology

Link to article, DOI:
10.1016/j.ejrad.2018.02.028

Publication date:
2018

Document Version
Publisher's PDF, also known as Version of record

European Journal of Radiology 103 (2018) 6–12

Contents lists available at ScienceDirect

European Journal of Radiology

journal homepage: www.elsevier.com/locate/ejrad

Research article

Combined hyperpolarized ^{13}C-pyruvate MRS and ^{18}F-FDG PET (hyperPET) estimates of glycolysis in canine cancer patients

Adam E. Hansen[a,*], Henrik Gutte[a], Pernille Holst[b], Helle H. Johannesen[a], Sofie Rahbek[a], Andreas E. Clemmensen[a], Majbritt M.E. Larsen[b], Christina Schøier[b], Jan Ardenkjaer-Larsen[c], Thomas L. Klausen[a], Annemarie T. Kristensen[b], Andreas Kjaer[a]

[a] Department of Clinical Physiology, Nuclear Medicine & PET and Cluster for Molecular Imaging, Rigshospitalet and University of Copenhagen, Denmark
[b] Department of Veterinary Clinical Sciences, Faculty of Health and Medical Sciences, University of Copenhagen, Frederiksberg C, Denmark
[c] Department of Electrical Engineering, Center for Hyperpolarization in Magnetic Resonance, Technical University of Denmark, Lyngby, Denmark

ARTICLE INFO

Keywords:
PET/MRI
MRS
Hyperpolarization
FDG-PET
Glycolysis

ABSTRACT

^{13}C Magnetic Resonance Spectroscopy (MRS) using hyperpolarized ^{13}C-labeled pyruvate as a substrate offers a measure of pyruvate-lactate interconversion and is thereby a marker of the elevated aerobic glycolysis (Warburg effect) generally exhibited by cancer cells. Here, we aim to compare hyperpolarized [1-^{13}C]pyruvate MRS with simultaneous ^{18}F-2-fluoro-2-deoxy-D-glucose (FDG) PET in a cross-sectional study of canine cancer patients.

Methods: Canine cancer patients underwent integrated PET/MRI using a clinical whole-body system. Hyperpolarized [1-^{13}C]pyruvate was obtained using dissolution-DNP. ^{18}F-FDG PET, dynamic ^{13}C MRS, ^{13}C MRS Imaging (MRSI) and anatomical ^{1}H MRI was acquired from 17 patients. Apparent pyruvate-to-lactate rate constants were estimated from dynamic ^{13}C MRS. ^{18}F-FDG Standard Uptake Values and maximum [1-^{13}C]lactate-to-total-^{13}C ratios were obtained from tumor regions of interest. Following inspection of data, patients were grouped according to main cancer type and linear regression between measures of lactate generation and ^{18}F-FDG uptake were tested within groups. Between groups, the same measures were tested for group differences.

Results: The main cancer types of the 17 patients were sarcoma (n = 11), carcinoma (n = 5) and mastocytoma (n = 1). Significant correlations between pyruvate-to-lactate rate constants and ^{18}F-FDG uptake were found for sarcoma patients, whereas no significant correlations appeared for carcinoma patients. The sarcoma patients showed a non-significant trend towards lower ^{18}F-FDG uptake and higher lactate generation than carcinoma patients. However, the ratio of lactate generation to ^{18}F-FDG uptake was found to be significantly higher in sarcoma as compared to carcinoma. The results were found both when lactate generation was estimated as an apparent pyruvate-to-lactate rate constant from dynamic ^{13}C MRS and as an [1-^{13}C]lactate to total ^{13}C ratio from ^{13}C MRSI.

Conclusions: A comparison of hyperpolarized [1-^{13}C]pyruvate MRS with simultaneous ^{18}F-FDG PET indicate that lactate generation and ^{18}F-FDG uptake in cancers can be related and that their relation depend on cancer type. This finding could be important for the interpretation and eventual clinical implementation of hyperpolarized ^{13}C. In addition, the differences between the two modalities may allow for better metabolic phenotyping performing hybrid imaging in the form of hyperPET.

1. Introduction

Clinical imaging of cancer has during the last decades witnessed morphological imaging modalities such as CT and MRI being supplemented and augmented by molecular imaging of tumor function [1–3]. PET offers whole-body functional imaging and ^{18}F-2-fluoro-2-deoxy-D-glucose (^{18}F-FDG) PET often in combination with diagnostic CT, is a widely used clinical tool for detection of cancer, staging and assessment of response to therapy [4–6]. FDG is a glucose analog, which is transported into cells and trapped as FDG-6-phosphate. The ^{18}F FDG uptake is a measure of regional glucose uptake and thereby an indirect marker of the elevated aerobic glycolysis, Warburg effect, generally exhibited by cancer cells [7,8].

Magnetic Resonance Spectroscopy (MRS) can also characterize cancer metabolism [9] and enabled by the development of dissolution Dynamic Nuclear Polarization (d-DNP) [10,11], hyperpolarized ^{13}C

* Corresponding author at: Department of Clinical Physiology, Nuclear Medicine & PET, Rigshospitalet, 3992, Blegdamsvej 9, DK-2100 Copenhagen Ø, Denmark.
E-mail address: adam.espe.hansen@regionh.dk (A.E. Hansen).

https://doi.org/10.1016/j.ejrad.2018.02.028
Received 5 November 2017; Received in revised form 13 February 2018; Accepted 24 February 2018

MRS has reached clinical accessibility. In particular, ^{13}C MRS Imaging (MRSI) of prostate cancer using hyperpolarized ^{13}C-labeled pyruvate as a substrate has been demonstrated in patients [12]. Here, the elevated aerobic glycolysis can be measured through the appearance of the ^{13}C-lactate signal, and dynamic ^{13}C MRS can provide an estimate of the apparent pyruvate-to-lactate rate constant. The measured rate constant is apparent since it is also affected by e.g. expression of monocarboxylic transporters in the cell membranes.

Accordingly, both ^{18}F FDG PET and hyperpolarized ^{13}C-pyruvate MRS are molecular imaging modalities sensitive to glycolysis. However, PET is well-established clinically while hyperpolarized MRS is still at its infancy [11,13–15]. The relation between ^{18}F FDG PET and hyperpolarized ^{13}C-pyruvate MRS in cancer has been explored in a limited number of preclinical studies using a sequential setup [13,16–18], focusing on feasibility [17] and treatment effects [13,16,18]. With the availability of integrated PET and MRI in a clinical, whole-body system [19], simultaneous PET and hyperpolarized ^{13}C MRS (hyperPET) [20,21] is possible. We have recently demonstrated, in a series of 10 canine cancer patients, an overall spatial concordance of ^{13}C-lactate and ^{18}F FDG uptake patterns [22], but have also observed canine cancer patients with a spatial mismatch [23]. Cancer cells utilize both glycolysis and oxidative phosphorylation for energy metabolism [8,24,25] and the degree of glycolysis might be heterogeneous across cancer cell types [24,26].

To further compare the two modalities of ^{18}F FDG PET and hyperpolarized ^{13}C-pyruvate MRS, we investigate in this study the relation between ^{18}F FDG uptake and apparent pyruvate-to-lactate rate constants in a larger series of canine cancer patients with different cancer types. This allows us to compare ^{18}F FDG PET and hyperpolarized ^{13}C-pyruvate MRS estimates of glycolysis in a cross-sectional study, with the very basic hypothesis that tumor ^{18}F FDG uptake and apparent pyruvate-to-lactate rate constants are correlated and may depend on cancer type.

2. Materials and methods

2.1. Study population

Seventeen canine cancer patients with solid tumors were consecutively enrolled in the study. All patients underwent physical examination as well as routine pre-anesthetic and diagnostic work up laboratory evaluation. Inclusion criteria were diagnosis of malignant tumor type and complete hyperPET data (^{18}F-FDG PET, dynamic ^{13}C MRS and ^{13}C MRSI). Exclusion criteria were clinical or laboratory work up precluding anesthesia. All canine cancer patients underwent PET/MRI with ^{18}F FDG PET as part of their diagnostic and staging work-up prior to therapy recommendation. Hyperpolarized ^{13}C MRSI was performed concomitantly. The owners gave informed consent and the study was approved by the Ethics and Administrative Committee, Department of Veterinary Clinical Sciences, Faculty of Health and Medical Sciences, University of Copenhagen.

2.2. Experimental setup

PET/MRI was performed using an integrated system (Siemens Biograph mMR) with a 3 T MR imager. ^{13}C MRSI utilized a ^{1}H/^{13}C dual-tuned transmit/receive surface flex coil centered on the lesion, or (patient 16, Table 1), a ^{13}C transmit/receive birdcage head coil (RAPID Biomedical).

The canine patients were anesthetized using a bolus injection of Propofol and maintained by administration of air/oxygen enriched gas mixture with Sevoflurane. Heart rate, oxygenation, and blood pressure were monitored throughout the scanning procedure.

Hyperpolarized [1-^{13}C]pyruvate was obtained using dissolution-DNP (SpinLab, GE Healthcare) using the procedure as described by Gutte et al. [22]. The amount injected was 0.68 mL/kg body weight of 250 mM [1-^{13}C]pyruvate.

2.3. ^{1}H-MRI

Anatomical ^{1}H MRI included T2 turbo spin echo (tse) [repetition time (TR) 4000 ms, echo time (TE) 89 ms, pixel size 0.6 × 0.5 mm^2, 19 slices of 3 mm thickness] in 3 planes. A single slice T2-tse angulated and centered as the ^{13}C MRSI was obtained as a geometrical reference. In most patients, the exam included transverse fat saturated T1-tse [TR 550 ms, TE 6.5 ms, pixel size 0.7 × 0.6 mm^2, 27 slices of 3 mm thickness] following gadolinium injection (0.1 mL/kg Gadovist).

Table 1
Summary of patient characteristics.

patient	weight [kg]	PET p.i. time [min]	Tumor location	Tumor tissue type	Grade	Classif. based on
1	15	42	Subcutaneous, face	Soft tissue sarcoma (Fibrosarcoma)	inter-mediate	Histo-pathology
2	42	41	Posterior paw	Soft tissue sarcoma	1	Histo-pathology
3	46	48	Nasal cavity	Squamous cell carcinoma	÷	Histo-pathology
4	50	26	Maxilla	Soft tissue sarcoma (Fibrosarcoma)	low	Histo-pathology
5	29	30	Nasal cavity	Chondrosarcoma	1	Histo-pathology
6	22	32	Scapula	Osteosarcoma – telangiectatic	2	Histo-pathology
7	13	39	Spine and axilla	Soft tissue sarcoma (pro peripheral nerve sheath)	2	Histo-pathology
8	21	78	Femur	Osteosarcoma – medullary	low	Histo-pathology
9	32	58	Thyroid	Carcinoma, follicular	n.r.	Histo-pathology
10	39	65	Axilla	Unspecified Sarcoma	÷	Cytology*
11	27	55	Thyroid	Adenocarcinoma – producing	n.r.	Histo-pathology
12	24	55	Thyroid	Carcinoma – C-cell	n.r.	Histo-pathology
13	19	60	Thyroid	Carcinoma, follicular	n.r.	Histo-pathology
14	48	61	Knee	Mastocytoma	2	Histo-pathology
15	33	58	Subcutaneous, thoracic wall	Soft tissue sarcoma	1	Histo-pathology
16	31	57	Trigeminal nerve	Pro soft tissue sarcoma – peripheral nerve sheath	÷	Imaging findings†
17	8	59	Maxillla	Soft tissue sarcoma (Fibrosarcoma)	low	Histo-pathology

n.r.: no relevant.
÷: not available.
* : The histopathological sample contained muscle cells only. Cytology showed malignantmesenchymal tumor cells, identifying the tumor as an unspecified sarcoma.
† : Initial diagnosis based on MRI findings prior to referral indicated neoplasia of the right trigeminal/mandibular nerve – most likely peripheral nerve sheath tumor (sarcoma). FDG-PET is consistent with neoplasia.

2.4. ^{18}F-FDG PET

PET was performed as a single-bed, 5 min acquisition, 30 min or 60 min post injection (p.i.) of 8 MBq/kg ^{18}F FDG.

Image reconstruction used 3D OP-OSEM with 4 iterations, 21 subsets, matrix 344 × 344, 4 mm 3D Gaussian post-filter and voxel size 2.1 × 2.1 × 2.0 mm^3. Attenuation correction (AC) utilized vendor supplied algorithm, however in some cases a faulty segmentation of the AC map was observed due to sensitivity profile of the MR surface coil, in which case a semi-automatic delineation of body contours to correct the AC map was performed based on the non-AC PET. ^{18}F FDG uptake was reported as standardized uptake values (SUV).

2.5. ^{13}C-MRS

Calibration of the ^{13}C MR flip angle was performed using an urea phantom [21].

Dynamic ^{13}C MRS [TR 1000 ms, TE 0.757 ms, flip angle 5°, bandwidth 4000 Hz, 180 repetitions, starting upon hyperpolarized ^{13}C-pyruvate injection] was recorded in an axially/oblique oriented 40 mm thick volume centered on and in most cases covering the entire tumor. The location of the volume was documented for the purpose of PET Region Of Interest (ROI) drawing.

^{13}C-MRSI employed 2D chemical shift imaging and was acquired 30–50 s p.i. of hyperpolarized [1-^{13}C]pyruvate [TR 80 ms, flip angle $\theta = 10^{\circ}$, bandwidth 10,000 Hz, slice thickness 13–23 mm, matrix 16 × 16, pixel size ranging from 5 × 5 mm^2 to 12.5 × 12.5 mm^2 and total imaging time 11 s]. Field-of-View was adjusted according to the body part of interest and planned through the central part of the tumor. The acquisition delay was chosen to obtain maximum ^{13}C-lactate signal based on the previous dynamic ^{13}C MRS acquisition. ^{13}C MRSI was obtained during or subsequent to PET.

2.6. Post processing of ^{13}C MRS

Peak areas of [1-^{13}C]pyruvate, [1-^{13}C]lactate, [1-^{13}C]alanine and [1-^{13}C]pyruvate hydrate were quantified using a general linear model implemented in MatLab (Mathworks) and applied in the time domain.

For the dynamic ^{13}C MRS, an apparent pyruvate-to-lactate rate constant k_{PL} was calculated as $k_{PL} = r_L \times AUC(lactate)/AUC(pyruvate)$, with the constant $r_L = {T_1}^{-1} - {T_R}^{-1} \times \ln(\cos(\theta))$ [27,28]. AUC refers to the area under the time series of the metabolite. T_1 was fixed at 20 s. Pyruvate delivery was characterized measuring Time To Peak (TTP) as well as Time To Initiation of the time series.

Concerning single time point ^{13}C MRSI, the metabolite ratio of lactate to all modeled peak heights (total Carbon) was calculated for all voxels which had both a lactate and a pyruvate peak height larger than 5 times the standard deviation of the noise in a background region of the spectrum. Ratio images were converted to DICOM for later ROI analysis.

2.7. ROI definition

Two sets of tumor PET ROIs were defined corresponding to the dynamic ^{13}C MRS acquisition and single time point ^{13}C MRSI, respectively.

The ROI corresponding to dynamic ^{13}C MRS was delineated based on a 50% of SUV_{max} iso-contour in Mirada XD (version 1.2.0.59, Mirada Medical) and limited to the ^{13}C MRS volume in case the volume did not cover the entire tumor. FDG uptake of non-neoplastic origin corresponding to e.g. muscle, joints, or nasal mucous membrane was removed. SUV_{mean}, SUV_{max} and ROI volume were recorded.

For the single time point ^{13}C MRSI, PET was resampled to the 2D imaging plane of the ^{13}C MRSI in OsiriX (version 4.1.2, PIXMEO) and the tumor was delineated as above. SUV_2D_{max} and the maximum lactate ratio $LactateRatio_{max}$ were recorded.

2.8. Comparison of ^{18}F FDG PET and hyperpolarized ^{13}C MRS

To explore the relation of FDG uptake and pyruvate-to-lactate interconversion, linear regression was tested for SUV_{mean}, SUV_{max} and 3D ROI volume versus k_{PL}, as well as SUV_2D_{max} versus $LactateRatio_{max}$. Further, the ratios $k_{PL}/SUV_{mean,max}$ and $LactateRatio_{max}/SUV\_2D_{max}$ were calculated for each lesion. Patients were grouped according to main cancer type following inspection of data. Group differences were assessed using a 2-sample unpaired *t*-test. A *p*-value of 0.05 was considered significant.

3. Results

3.1. Patients

Seventeen canine cancer patients were included. Six patients had PET acquired nominally 30 min p.i. (all sarcoma), and 11 patients 60 min p.i. (patient 3 had PET delayed to 48 min p.i and was included in the 60 min p.i. group). Cancer types included seven soft tissue (ST) sarcomas, four thyroid carcinomas, two osteosarcomas, one chondrosarcoma, one unspecified sarcoma, one mastocytoma and one squamous cell (SC) carcinoma. Tumor classification was based on histopathology except for patient 10 and 16, which were diagnosed by cytology and combined clinical and imaging findings, respectively (Table 1).

3.2. Patient examples

Fig. 1 shows a patient with a large thyroid carcinoma and Fig. 2 a patient with a fibrosarcoma extending from the maxilla to behind the left eye. The tumors exhibited FDG uptake [subfigures a) and c)] as well as lactate signal both during dynamic ^{13}C MRS [subfigures b)] and with single time point ^{13}C MRSI [subfigures d)].

3.3. Comparison of apparent lactate generation and ^{18}F FDG uptake

The apparent pyruvate-to-lactate rate constant k_{PL} obtained from all canine patients varied by a factor of more than 10. Fig. 3a)–c) shows SUV_{mean}, SUV_{max} and Volume from the 3D ROI as function of k_{PL}. Cancer type is denoted in the legend of Fig. 3a). There is clearly no correlation between apparent pyruvate-to-lactate rate constants and ^{18}F FDG uptake across patients with all cancer types, Fig. 3a)–b). Upon closer inspection, two main qualitative features can be seen immediately: 1) The sarcoma patients tend to show a linear relation between SUV and k_{PL} across patients, both for PET data obtained 30 min p.i. (filled grey symbols) and 60 min p.i. (filled black symbols). The trend is observed across sarcoma cancer subtypes. No linear trend appears for carcinoma patients. 2) In the group of patients with sarcoma, patients appear to have a combination of lower SUV and higher k_{PL} than the carcinoma (open triangles and square). Of further note, the mastocytoma (open diamond) appears to group with the sarcoma patients. The tumor volume appears unrelated to k_{PL}. The qualitative trends 1)-2) are replicated by the 2D measurements of maximum lactate ratio and SUV_2D_{max} in the ^{13}C MRSI imaging plane shown in Fig. 4.

Results of testing for linear trends between ^{18}F FDG uptake and lactate generation across patients are shown in Table 2 confirming the qualitative impressions above. Significant slopes appear for k_{PL} versus SUV_{max} (sarcomas 30 and 60 min p.i.), k_{PL} versus SUV_{mean} (sarcomas 60 min p.i.) and $LactateRatio_{max}$ versus SUV_2D_{max} (sarcomas 60 min p.i.). Also, k_{PL} versus SUV_{mean} (sarcomas 30 min p.i.) is close to significance ($p = 0.064$). No linear relation involving the group of carcinomas is significant; neither is the relation of k_{PL} and tumor volume. No offsets are significant for any of the linear trends tested. Regression lines for significant correlations are included in Figs. 3 and 4.

The qualitative impression that sarcoma patients showed a combination of higher apparent lactate generation and lower ^{18}F FDG uptake

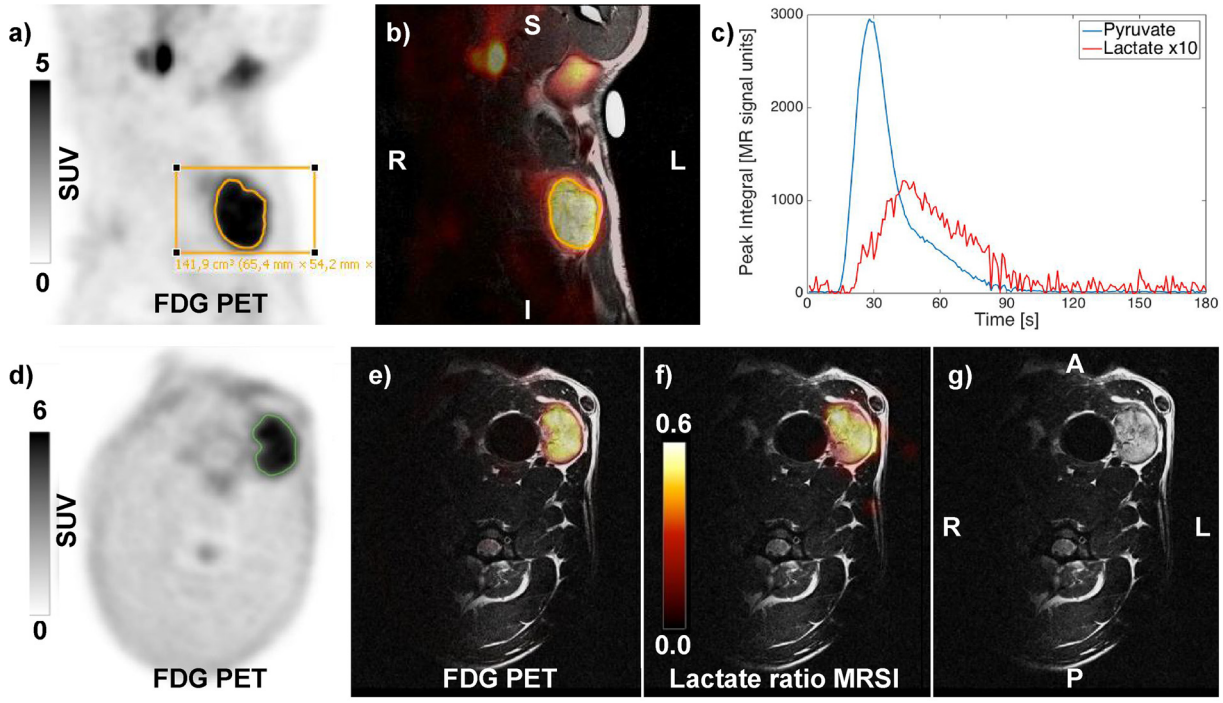

Fig. 1. Carcinoma patient example.
Figure shows patient 9 (Table 1). ^{18}F FDG PET in a) coronal orientation with 3D ROI (outlined in orange) and b) fused with T2-tse MRI. c) Pyruvate (blue) and lactate (red, multiplied by 10) peak areas as function of time from injection of hyperpolarized pyruvate. d) ^{18}F FDG PET in the transverse orientation of the ^{13}C MRSI plane with 2D ROI (outlined in green) and e) fused with T2-tse MRI. f) Lactate ratio from ^{13}C MRSI fused with T2-tse MRI and g) T2-tse MRI.

than sarcoma patients was tested by comparing ratios of apparent pyruvate-to-lactate rate constant k_{PL} to SUV_{mean} and SUV_{max} and likewise the ratio of $LactateRatio_{max}$ to SUV_2D_{max} in patients with ^{18}F FDG PET obtained 60 min p.i. Results are shown in Table 3 Fig. 5. The ratios k_{PL}/SUV_{mean} and k_{PL}/SUV_{max} were significantly higher (on average by a factor of approximately 3, p = 0.001 and 0.003) in the group of sarcoma patients as compared to the carcinoma patients. The tendencies to higher k_{PL} and a lower $SUV_{mean,max}$ in sarcoma as compared to carcinoma were not statistically significant. Also, the ratio $LactateRatio_{max}/SUV\_2D_{max}$ was significantly higher (on average by a factor of approximately 3, p = 0.001) in the group of sarcoma patients as compared to the carcinoma patients (Fig. 5).

Pyruvate TTP was 24.9 ± 6.6 s. TTP, TTI and TTP-TTI were not significantly different between groups of sarcoma and carcinoma patients.

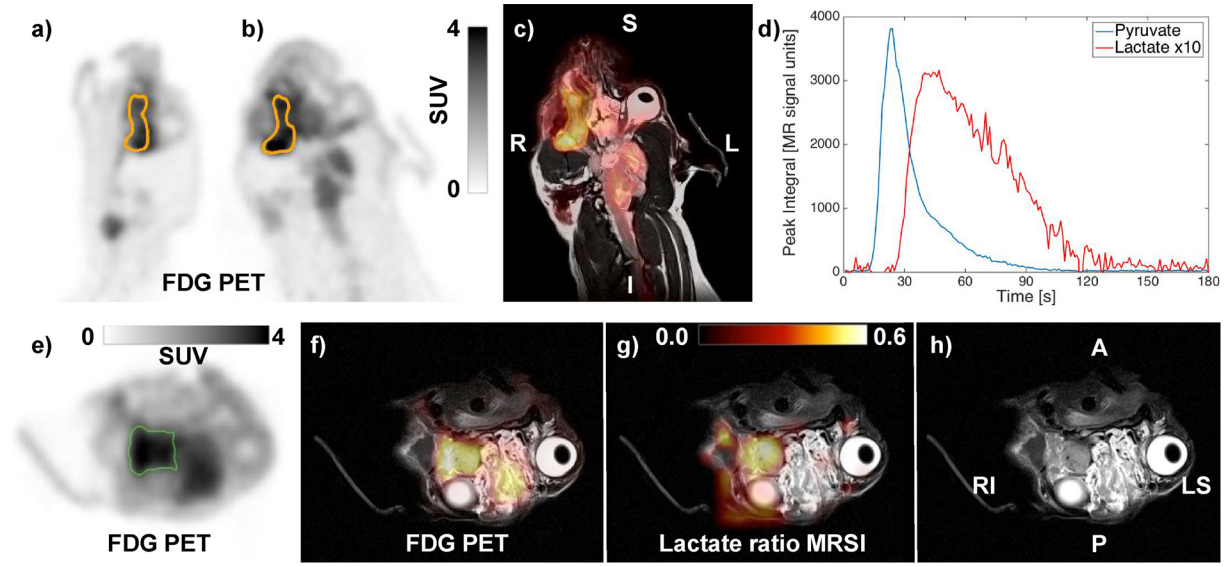

Fig. 2. Sarcoma patient example.
Figure shows patient 17 (Table 1). ^{18}F FDG PET in a) sagittal and b) coronal orientation with 3D ROI (outlined in orange color) and c) fused with T2-tse MRI. d) Pyruvate (blue) and lactate (red, multiplied by 10) peak areas. e) ^{18}F FDG PET in the transverse/oblique orientation of the ^{13}C MRSI plane with 2D ROI (outlined in green color) and f) fused with T2-tse MRI. g) Lactate ratio from ^{13}C MRSI fused with T2-tse MRI and h) T2-tse MRI.

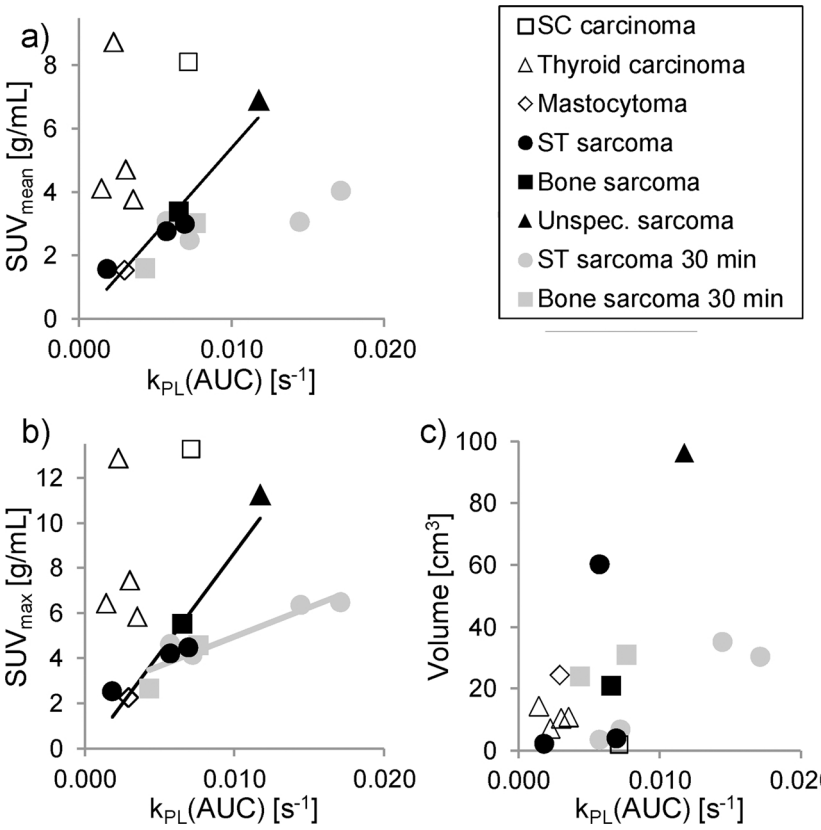

Fig. 3. Correlation of FDG uptake and lactate generation. Figure shows tumor ^{18}F FDG uptake quantified as SUVmean (subfigure a), SUVmax (subfigure b) and ROI Volume (subfigure c) versus apparent pyruvate-to-lactate transfer coefficient k_{PL}. Cancer types are explained in the legend (subfigure a). Lines show linear trends for significant correlations within main cancer types (sarcoma and carcinoma) (see Table 2).

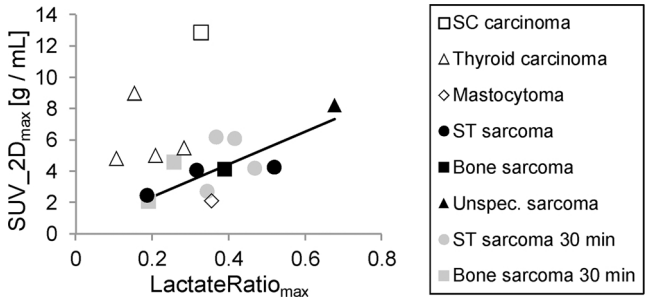

Fig. 4. Correlation of FDG uptake and lactate generation, 2D ROI. Figure shows tumor SUV_2Dmax in the 2D plane of the ^{13}C MRSI versus maximum tumor lactate to pyruvate ratio, $LactateRatio_{max}$. Grouping of patients and symbols used are the same as in Fig. 3, and are explained in the legend. The line shows the linear trend for a significant correlation in the group of sarcoma patients (Table 2).

Table 2
Correlation of [1-^{13}C]lactate generation and ^{18}F FDG uptake.

Cancer type	Sarcoma		Carcinoma
Nominal PET uptake time [p.i.]	30 min (n = 6)	60 min (n = 5)	60 min (n = 5)
Correlation of k_{PL} and SUV_{max}	p = 0.008* R^2 = 0.85	p = 0.016* R^2 = 0.89	p = 0.37 R^2 = 0.21
Correlation of k_{PL} and SUV_{mean}	p = 0.064 R^2 = 0.62	p = 0.011* R^2 = 0.92	p = 0.46 R^2 = 0.14
Correlation of k_{PL} and Volume	p = 0.22 R^2 = 0.35	p = 0.13 R^2 = 0.77	p = 0.19 R^2 = 0.38
Correlation of $(Lac/Pyr)_{max}$ and SUV_{max}	p = 0.23 R^2 = 0.27	p = 0.033* R^2 = 0.83	p = 0.34 R^2 = 0.30

Uncorrected R2 values for linear regression are reported.
* P < 0.05.

Table 3
Group differences of [1-^{13}C]lactate generation and ^{18}F FDG uptake.

	Carcinoma (n = 5)	Sarcoma (n = 5)	Difference
k_{PL} [s^{-1}]	(3.44 ± 2.20)*10^{-3}	(6.52 ± 3.53)*10^{-3}	p = 0.144
SUV_{mean} [g/mL]	5.90 ± 2.35	3.52 ± 2.02	p = 0.125
SUV_{max} [g/mL]	9.20 ± 3.60	5.60 ± 3.34	p = 0.140
k_{PL}/SUV_{mean} [$s^{-1}g^{-1}mL$]	(0.605 ± 0.305)*10^{-3}	(1.82 ± 0.439)*10^{-3}	p = 0.001*
k_{PL}/SUV_{max} [$s^{-1}g^{-1}mL$]	(0.384 ± 0.188)*10^{-3}	(1.16 ± 0.317)*10^{-3}	p = 0.003*
$LactateRatio_{max}$	0.215 ± 0.091	0.418 ± 0.188	p = 0.075
SUV_2D_{max} [g/mL]	7.44 ± 3.46	4.64 ± 2.15	p = 0.170
$LactateRatio_{max}/SUV\_2D_{max}$ [$g^{-1}mL$]	0.0314 ± 0.0143	0.0903 ± 0.0190	p = 0.001*

All PET data are obtained nominally 60 min p.i. Average values ± standard deviations are reported.
* P < 0.05.

4. Discussion

The study compared measurements of elevated aerobic glycolysis by means of ^{18}F FDG PET and hyperpolarized [1-^{13}C]pyruvate MRS in a series of canine patients with solid tumors of different tissue types. The combination of pyruvate-to-lactate rate constants and ^{18}F FDG uptake appeared to group patients according to main cancer types. Thus, the ratio of apparent pyruvate-to-lactate rate constant to ^{18}F FDG uptake was found to be significantly higher in sarcoma as compared to carcinoma. Pyruvate-to-lactate rate constants and ^{18}F FDG uptake correlated well across patients in the sarcoma patient group, but not in the carcinoma patient group. Those results indicate that while lactate generation and ^{18}F FDG uptake in cancers can be related, their relation depends on cancer tissue type. This finding could be important for the interpretation and eventual clinical implementation of hyperpolarized

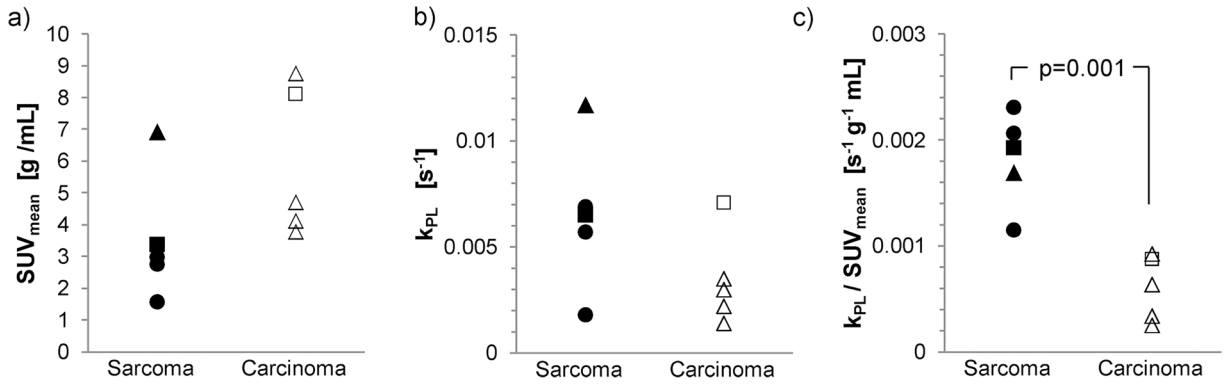

Fig. 5. Group differences of FDG uptake and lactate generation.
Differences of SUVmean (subfigure a), apparent pyruvate-to-lactate transfer coefficient k_{PL} (subfigure b) and k_{PL}/SUVmean (subfigure c) between groups of carcinoma and sarcoma patients are illustrated. Only k_{PL}/SUVmean shows a significant group difference (p-values are reported in Table 3). All PET data are obtained nominally 60 min p.i. Symbols are the same as in Figs. 3 and 4.

^{13}C pyruvate imaging.

Only a few earlier studies have compared ^{18}F FDG PET and hyperpolarized [1-^{13}C]pyruvate MRS in animal models [16,17], and using sequential exams as opposed to simultaneous exams performed by us in the combined PET/MR clinical system. In a study of murine lymphoma treatment [16], a comparable decrease in ^{18}F FDG uptake and pyruvate-to-lactate exchange was found 24 h after chemotherapy, with the decrease in ^{18}F FDG uptake appearing earliest. A recent treatment study using an ovarian cancer mouse model showed increased pyruvate-to-lactate conversion after chemotherapy without a change in ^{18}F FDG uptake [18]. There was no attempt to correlate ^{18}F FDG uptake and ^{13}C MRS across animals in the abovementioned studies. In a study of hepatocellular carcinoma tumor–bearing rats [17], tumors exhibited increased ^{18}F FDG uptake and locally increased pyruvate-to-lactate exchange. However, no correlation between PET and MRS data was observed across animals, possibly corresponding to the lack of correlation we observe for the canine carcinoma patients. Previous studies on canine cancer patients from our group [20,22,23] focused on single cases, feasibility and spatial concordance of ^{18}F FDG PET and hyperpolarized [1-^{13}C]pyruvate MRSI and did not compare data across patients or cancer tissue types.

The apparent pyruvate-to-lactate rate constant reported here was based on dynamic measurements performed in a 40 mm thick slab encompassing the tumor but also surrounding tissues which may influence rate constant estimates. This methodology is common in the field of hyperpolarized ^{13}C MRS. The overall pattern in the relation between ^{18}F FDG uptake and lactate generation (linear relation between measures for sarcoma but not carcinoma, higher ratio of lactate generation to ^{18}F FDG uptake in sarcoma as compared to carcinoma, Fig. 3a, b) was reproduced by measurements based on single time point ^{13}C MRS imaging (Fig. 4). This supports the robustness of the findings. The tumors of the present study showed a large heterogeneity of anatomic location which could influence delivery of the hyperpolarized pyruvate substrate; however the delivery times were not different between tumor types. Lactate can also be detected by ^{1}H MRS [9] but hyperpolarized ^{13}C MRS provides information on the dynamics of lactate generation, which may be advantageous in the assessment of alterations of tumor cell energy metabolism [33]. Dynamic acquisition of FDG-PET with arterial blood sampling, which would have enabled kinetic modelling of FDG uptake, was not feasible with the present patient setup. Overall, significant correlations of pyruvate-to-lactate rate constants and ^{18}F FDG uptake appear irrespective of FDG uptake time (Fig. 3 and Table 2), suggesting that kinetic modelling would not alter the conclusions of the study.

We may speculate on why the ratio of lactate generation and ^{18}F FDG uptake was different for sarcoma and carcinoma in context of the origin of the Warburg effect. The aerobic glycolysis generally exhibited by cancer cells can occur while the cells still use glucose to produce ATP in the mitochondria [8,24,25,29]. Accordingly, the relative contribution of aerobic glycolysis and oxidative phosphorylation may vary [24,26]. Therefore, the different relation between ^{18}F FDG uptake and lactate generation in different cancer tissue types may be interpreted as a metabolic signature of the relative contribution from the Warburg effect. If this interpretation can be confirmed by independent experiments including ex vivo validation, the relation between ^{18}F FDG uptake and lactate generation may be used to shed further light on the origins of the Warburg effect [30,31].

From a clinical perspective, the question naturally arises whether ^{18}F FDG PET and [1-^{13}C]pyruvate MRSI provides similar or complementary information. Based on the present study we can hypothesize that the combination of ^{18}F FDG PET and hyperpolarized [1-^{13}C]pyruvate MRSI (hyperPET), but not the modalities alone, can characterize regulation of glycolysis. Reprogramming of energy metabolism has been proposed as a Hallmark of Cancer [32] and thus hyperPET may provide a new method of better metabolic cancer phenotyping. However, a possible clinical role of such improved phenotyping by hyperPET will need to be investigated in future human studies.

HyperPET data from six of the canine cancer patients included here was already reported by our group in [20,22]. However, due to the small number of animals the cross-sectional comparison of ^{18}F FDG PET and ^{13}C MRS as presented here was not attempted.

The present study population showed a large heterogeneity of cancer types, lactate generation rate and ^{18}F FDG uptake. Such heterogeneity is also a common feature of clinical cancer patients and was likely beneficial to explore main differential characteristics of ^{18}F FDG PET and hyperpolarized ^{13}C MRS. However, the heterogeneity together with low to intermediate grades hampered a comparison between cancer grade and imaging findings. The correlation of FDG uptake and apparent pyruvate-to-lactate rate constants was evaluated grouping patients according to main cancer tissue types (carcinoma, sarcoma). While soft tissue sarcoma and bone sarcoma appeared to follow a common trend line, this very rough classification may be the reason why no correlation was observed for the group of carcinoma patients.

Clearly, with the small number of animals and the limited number of cancer tissue types, the present data should be viewed as hypothesis generating only. Overall, combined PET/MRI using ^{13}C hyperpolarized probes seem valuable to improve metabolic phenotyping in cancer.

5. Conclusion

Comparing ^{18}F FDG PET and ^{13}C MRS apparent pyruvate-to-lactate rate constants we found correlation within certain tumor tissue types but not across tumor types. As ^{13}C MRS apparent pyruvate-to-lactate transfer most likely is the best reflection of aerobic glycolysis (Warburg

effect) this demonstrates that ^{18}F FDG PET cannot in general be regarded as a clear indicator of the Warburg effect, but within certain tumor tissue types and microenvironment conditions there may be a strong correlation. The differences between the two modalities may allow for better metabolic phenotyping performing hybrid imaging in the form of hyperPET.

Conflict of interest

All authors have no conflicts of interest and no disclosures of financial interest to report.

Acknowledgements

The financial support from the John and Birthe Meyer Foundation, the Capital Region of Denmark, the Novo Nordisk Foundation, the Lundbeck Foundation, the Innovation Fund Denmark, the Research Council for Independent Research and the Danish National Research Foundation (DNRF124) is gratefully acknowledged.

References

[1] R.L. Wahl, H. Jacene, Y. Kasamon, M.A. Lodge, From RECIST to PERCIST: evolving considerations for PET response criteria in solid tumors, J. Nucl. Med. 50 (Suppl. 1) (2009) 122S–150S, http://dx.doi.org/10.2967/jnumed.108.057307.

[2] B. Fischer, U. Lassen, J. Mortensen, S. Larsen, A. Loft, A. Bertelsen, J. Ravn, P. Clementsen, A. Hogholm, K. Larsen, T. Rasmussen, S. Keiding, A. Dirksen, O. Gerke, B. Skov, I. Steffensen, H. Hansen, P. Vilmann, G. Jacobsen, V. Backer, N. Maltbaek, J. Pedersen, H. Madsen, H. Nielsen, L. Hojgaard, Preoperative staging of lung cancer with combined PET-CT, N. Engl. J. Med. 361 (2009) 32–39, http://dx.doi.org/10.1056/NEJMoa0900043.

[3] T. Binderup, U. Knigge, A. Loft, B. Federspiel, A. Kjaer, F-18-Fluorodeoxyglucose positron emission tomography predicts survival of patients with neuroendocrine tumors, Clin. Cancer Res. 16 (2010) 978–985, http://dx.doi.org/10.1158/1078-0432.CCR-09-1759.

[4] S.S. Gambhir, Molecular imaging of cancer with positron emission tomography, Nat. Rev. Cancer 2 (2002) 683–693, http://dx.doi.org/10.1038/nrc882.

[5] J.W. Fletcher, B. Djulbegovic, H.P. Soares, B.A. Siegel, V.J. Lowe, G.H. Lyman, R.E. Coleman, R. Wahl, J.C. Paschold, N. Avril, L.H. Einhorn, W.W. Suh, D. Samson, D. Delbeke, M. Gorman, A.F. Shields, Recommendations on the use of 18F-FDG PET in oncology, J. Nucl. Med. 49 (2008) 480–508, http://dx.doi.org/10.2967/jnumed.107.047787.

[6] M.D. Farwell, D.A. Pryma, D.A. Mankoff, PET/CT imaging in cancer: current applications and future directions, Cancer 120 (2014) 3433–3445, http://dx.doi.org/10.1002/cncr.28860.

[7] O. Warburg, On the origin of cancer cells, Science 123 (1956) 309–314, http://dx.doi.org/10.1126/science.123.3191.309.

[8] W.H. Koppenol, P.L. Bounds, C.V. Dang, Otto Warburg's contributions to current concepts of cancer metabolism, Nat. Rev. Cancer 11 (2011) 325–337, http://dx.doi.org/10.1038/nrc3038.

[9] R.J. Gillies, D.L. Morse, In vivo magnetic resonance spectroscopy in cancer, Annu. Rev. Biomed. Eng. 7 (2005) 287–326, http://dx.doi.org/10.1146/annurev.bioeng.7.060804.100411.

[10] J.H. Ardenkjaer-Larsen, B. Fridlund, A. Gram, G. Hansson, L. Hansson, M.H. Lerche, R. Servin, M. Thaning, K. Golman, Increase in signal-to-noise ratio of > 10 000 times in liquid-state NMR, Proc. Natl. Acad. Sci. U. S. A. 100 (2003) 10158–10163, http://dx.doi.org/10.1073/pnas.1733835100.

[11] A. Comment, M.E. Merritt, Hyperpolarized magnetic resonance as a sensitive detector of metabolic function, Biochemistry 53 (2014) 7333–7357, http://dx.doi.org/10.1021/bi501225t.

[12] S. Nelson, J. Kurhanewicz, D. Vigneron, P. Larson, A. Harzstark, M. Ferrone, M. van Criekinge, J. Chang, R. Bok, I. Park, G. Reed, L. Carvajal, E. Small, P. Munster, V. Weinberg, J. Ardenkjaer-Larsen, A. Chen, R. Hurd, L. Odegardstuen, F. Robb, J. Tropp, J. Murray, Metabolic imaging of patients with prostate cancer using hyperpolarized [1-^{13}C]pyruvate, Sci. Transl. Med. 5 (2013) 198ra108, http://dx.doi.org/10.1126/scitranslmed.3006070.

[13] F. a Gallagher, S.E. Bohndiek, M.I. Kettunen, D.Y. Lewis, D. Soloviev, K.M. Brindle, Hyperpolarized 13C MRI and PET: in vivo tumor biochemistry, J. Nucl. Med. 52 (2011) 1333–1336, http://dx.doi.org/10.2967/jnumed.110.085258.

[14] H. Gutte, A.E. Hansen, H.H. Johannesen, A.E. Clemmensen, J.H. Ardenkjaer-Larsen, C.H. Nielsen, A. Kjaer, J. Henrik, The use of dynamic nuclear polarization (13)C-pyruvate MRS in cancer, Am. J. Nucl. Med. Mol. Imaging 5 (2015) 548–560.

[15] A. Cho, J.Y.C. Lau, B.J. Geraghty, C.H. Cunningham, K.R. Keshari, Noninvasive interrogation of cancer metabolism with hyperpolarized 13C magnetic resonance imaging, J. Nucl. Med. 58 (2017) 1201–1206, http://dx.doi.org/10.2967/jnumed.116.182170 jnumed.116.182170.

[16] T.H. Witney, M.I. Kettunen, S.E. Day, D. Hu, A.A. Neves, F.A. Gallagher, S.M. Fulton, K.M. Brindle, A comparison between radiolabeled fluorodeoxyglucose uptake and hyperpolarized (13)C-labeled pyruvate utilization as methods for detecting tumor response to treatment, Neoplasia 11 (2009) 574–582, http://dx.doi.org/10.1593/neo.09254.

[17] M.I. Menzel, E.V. Farrell, M. a Janich, O. Khegai, F. Wiesinger, S. Nekolla, A.M. Otto, A. Haase, R.F. Schulte, M. Schwaiger, Multimodal assessment of in vivo metabolism with hyperpolarized [1–13C]MR spectroscopy and 18F-FDG PET imaging in hepatocellular carcinoma tumor-bearing rats, J. Nucl. Med. 54 (2013) 1113–1119, http://dx.doi.org/10.2967/jnumed.112.110825.

[18] M.K. Ravoori, S.P. Singh, J. Lee, J.A. Bankson, V. Kundra, In vivo assessment of ovarian tumor response to tyrosine kinase inhibitor pazopanib by using hyperpolarized 13C-pyruvate MR spectroscopy and 18F-FDG PET/CT imaging in a mouse model, Radiology 285 (2017) 1–9, http://dx.doi.org/10.1148/radiol.2017161772.

[19] G. Delso, S. Fürst, B. Jakoby, R. Ladebeck, C. Ganter, S.G. Nekolla, M. Schwaiger, S.I. Ziegler, Performance measurements of the Siemens mMR integrated whole-body PET/MR scanner, J. Nucl. Med. 52 (2011) 1914–1922, http://dx.doi.org/10.2967/jnumed.111.092726.

[20] H. Gutte, Hansen A.E.A.E.A.E, S.T. Henriksen, H.H. Johannesen, J. Ardenkjaer-Larsen, A. Vignaud, A.E.A.E.A.E. Hansen, B. Borresen, T.L. Klausen, A.-M.N. Wittekind, N. Gillings, A.T. Kristensen, A. Clemmensen, L. Hojgaard, A. Kjaer, B. Børresen, T.L. Klausen, A.-M.N. Wittekind, N. Gillings, A.T. Kristensen, A. Clemmensen, L. Højgaard, A. Kjær, B. Borresen, T.L. Klausen, A.-M.N. Wittekind, N. Gillings, A.T. Kristensen, A. Clemmensen, L. Hojgaard, A. Kjaer, Simultaneous hyperpolarized (13)C-pyruvate MRI and (18)F-FDG-PET in cancer (hyperPET): feasibility of a new imaging concept using a clinical PET/MRI scanner, Am. J. Nucl. Med. Mol. Imaging 5 (2015) 38–45 http://www.pubmedcentral.nih.gov/articlerender.fcgi?artid=4299777&tool=pmcentrez&rendertype=abstract.

[21] A.E. Hansen, F.L. Andersen, S.T. Henriksen, A. Vignaud, J.H. Ardenkjaer-Larsen, L. Højgaard, A. Kjaer, T.L. Klausen, Simultaneous PET/MRI with (13)C magnetic resonance spectroscopic imaging (hyperPET): phantom-based evaluation of PET quantification, EJNMMI Phys. 3 (2016) 7, http://dx.doi.org/10.1186/s40658-016-0143-6.

[22] H. Gutte, A.E. Hansen, M.M.E. Larsen, S. Rahbek, S.T. Henriksen, H.H. Johannesen, J. Ardenkjaer-Larsen, A.T. Kristensen, L. Hojgaard, A. Kjaer, Simultaneous hyperpolarized 13C-pyruvate MRI and 18F-FDG PET (HyperPET) in 10 dogs with cancer, J. Nucl. Med. 56 (2015) 1786–1792, http://dx.doi.org/10.2967/jnumed.115.156364.

[23] H. Gutte, A.E. Hansen, M.M.E. Larsen, S. Rahbek, H.H. Johannesen, J. Ardenkjaer-larsen, A.T. Kristensen, L. Højgaard, A. Kjaer, In vivo phenotyping of tumor metabolism in a canine cancer patient with simultaneous 18F-FDG-PET and hyperpolarized 13C-pyruvate magnetic resonance spectroscopic imaging (hyperPET): mismatch demonstrates that FDG may not always reflect the warburg effect, Diagnostics 5 (2015) 287–289, http://dx.doi.org/10.3390/diagnostics5030287.

[24] X.L. Zu, M. Guppy, Cancer metabolism: facts, fantasy, and fiction, Biochem. Biophys. Res. Commun. 313 (2004) 459–465, http://dx.doi.org/10.1016/j.bbrc.2003.11.136.

[25] R.J. DeBerardinis, N.S. Chandel, Fundamentals of cancer metabolism, Sci. Adv. 2 (2016) e1600200, http://dx.doi.org/10.1126/sciadv.1600200.

[26] M. Potter, E. Newport, K.J. Morten, The Warburg effect: 80 years on, Biochem. Soc. Trans. 44 (2016) 1499–1505, http://dx.doi.org/10.1042/BST20160094.

[27] D.K. Hill, M.R. Orton, E. Mariotti, J.K.R. Boult, R. Panek, M. Jafar, H.G. Parkes, Y. Jamin, M.F. Miniotis, N.M.S. Al-Saffar, M. Beloueche-Babari, S.P. Robinson, M.O. Leach, Y.L. Chung, T.R. Eykyn, Model free approach to kinetic analysis of real-time hyperpolarized 13C magnetic resonance spectroscopy data, PLoS One 8 (2013) 1–10, http://dx.doi.org/10.1371/journal.pone.0071996.

[28] C.J. Daniels, M.A. McLean, R.F. Schulte, F.J. Robb, A.B. Gill, N. McGlashan, M.J. Graves, M. Schwaiger, D.J. Lomas, K.M. Brindle, F.A. Gallagher, A comparison of quantitative methods for clinical imaging with hyperpolarized 13C -pyruvate, NMR Biomed. 29 (2016) 387–399, http://dx.doi.org/10.1002/nbm.3468.

[29] C.T. Hensley, B. Faubert, Q. Yuan, N. Lev-Cohain, E. Jin, J. Kim, L. Jiang, B. Ko, R. Skelton, L. Loudat, M. Wodzak, C. Klimko, E. McMillan, Y. Butt, M. Ni, D. Oliver, J. Torrealba, C.R. Malloy, K. Kernstine, R.E. Lenkinski, R.J. DeBerardinis, Metabolic heterogeneity in human lung tumors, Cell 164 (2016) 681–694, http://dx.doi.org/10.1016/j.cell.2015.12.034.

[30] R.J. Gillies, I. Robey, R.A. Gatenby, Causes and consequences of increased glucose metabolism of cancers, J. Nucl. Med. 49 (Suppl. 2) (2008) 24S–42S, http://dx.doi.org/10.2967/jnumed.107.047258.

[31] S. Pavlides, D. Whitaker-Menezes, R. Castello-Cros, N. Flomenberg, A.K. Witkiewicz, P.G. Frank, M.C. Casimiro, C. Wang, P. Fortina, S. Addya, R.G. Pestell, U.E. Martinez-Outschoorn, F. Sotgia, M.P. Lisanti, The reverse Warburg effect: aerobic glycolysis in cancer associated fibroblasts and the tumor stroma, ABBV Cell Cycle 8 (2009) 3984–4001, http://dx.doi.org/10.4161/cc.8.23.10238.

[32] D. Hanahan, R.A. Weinberg, Hallmarks of cancer: the next generation, Cell 144 (2011) 646–674, http://dx.doi.org/10.1016/j.cell.2011.02.013.

[33] K.M. Brindle, S.E. Bohndiek, F.A. Gallagher, M.I. Kettunen, Tumor imaging using hyperpolarized 13C magnetic resonance spectroscopy, Magn. Reson. Med. 66 (2011) 505–519, http://dx.doi.org/10.1002/mrm.22999.